Graphene-integrated $CuCo_2S_4$ microspheres as a sustainable anode material for Li-ion batteries with improved storage capacity

Abu Talha Aqueel Ahmed,[1] Akbar I. Inamdar,[1] S. M. Pawar,[1] Bo Hou,[2] SeungNam Cha,[3] Hyungsang Kim,*[1] Hyunsik Im*[1]

[1]Division of Physics and Semiconductor Science, Dongguk University, Seoul 04620, South Korea

[2]Department of Engineering Science, University of Oxford, Parks Road, OX1 3PJ, UK

[3]Department of Physics, Sungkyunkwan University, Suwon, 16419, Republic of Korea

E–mail: hskim@dongguk.edu, hyunsik7@dongguk.edu

Abstract

Current graphite anodes (theoretical capacity: 372 mAh g^{-1}) for lithium-ion batteries (LIBs) are insufficient to bridge the energy density gap between demand and supply in advanced heavy and portable electronic devices. Ternary chalcogenide metal-sulfides are promising as alternative anode materials in high power and energy densities but suffer from capacity fading with poor long-term cycling stability due to the dissolution of polysulfide species created during the lithium-ion insertion/de-insertion process. Here, we report the hydrothermal synthesis of graphene integrated $CuCo_2S_4$ microparticles as a high-capacity and sustainable anode material for LIBs. We solve the concentration gradient of lithium polysulfide at the electrolyte/electrode interface via integrating graphene into the active metal sulfide anode material. The mechanically flexible and highly conductive nature of graphene helps relieve undesirable elongation and shrinkage during battery cycling suppressing active material dissolution and enhances electron

transport. Our one step approach demonstrates towards the practical application of advanced metal sulfide anodes for LIBs.

Keywords: Lithium-ion batteries, $CuCo_2S_4$, reduced graphene oxide, hydrothermal growth

1. Introduction

In general, a battery consists of four core elements (anode, cathode, electrolyte and separator). The optimized combination of these elements could deliver maximum energy density, which is essential to address the rapidly increasing energy demand in emerging technologies. Batteries with high output energy densities could be obtained by developing high-voltage cathode materials or high-capacity cathode/anode materials [1]. Present commercial lithium-ion batteries (LIBs) consist mainly of lithium cobalt oxide as the cathode material, and graphite-based carbonaceous materials which are the most popular anode materials [2]. However, a graphite anode is not suitable as a LIB anode material for advanced electronic devices because of the limited theoretical capacity (372 mAh g^{-1}) [3,4]. Therefore, substantial efforts have been made to develop high-capacity substitutes with safety and reliability for conventional carbon anode materials via hybridizing materials, nanotechnologies, synthesizing novel compound materials, etc [5-7].

Because of their earth-abundance (or low material cost), superior thermal/chemical stability, and good structural robustness, various metal sulfide materials, specially $CuCo_2S_4$ have attracted considerable attention as promising substitutes for current graphite-based LIB anodes [8-21]. The low electronegativity of sulfur (S) could provide structural flexibility in the active anode material during lithium-ion (Li^+) intercalation/ deintercalation processes resulting in good Li^+ storage

without undesirable volume expansion [6,22,23]. However, metal sulfide anode possesses poor endurance performance upon cycling caused by active material dissolution during the discharge/charge process. The general lithiation and de-lithiation mechanism of metal sulfides with Li^+ is defined as follows [24]:

$$M^{n+}S + ne^- + nLi^+ \leftrightarrow M^o + nLiS, \quad (1)$$

where M represents a constituent metal. The conversion of lithium polysulfide (Li_2S_x, where $6 < x \leq 8$) into smaller Li_2S_x ($2 < x \leq 6$) during the discharge/charge reactions leads to the dissolution of the polysulfide anions into the electrolyte because of their high solubility in organic solvent electrolytes [25,26]. Consequently, the formation of a concentration gradient forces the anion to move in the opposite direction of Li^+ across the separator, resulting in the capacity fading of the active anode material. This capacity fading issue can be solved via graphene incorporation. A highly flexible and conductive nature of graphene helps release unwanted elongation/shrinkage upon cycling reducing active material dissolution and improves electron transport. In order to solve the capacity fading issue of metal sulfide-based anodes, Tian et al. reported porous core-shell $CuCo_2S_4$ nanospheres as an anode material whose first discharge capacity is 1599.9 mAh/g at 1 A/g but decreases rapidly to approximately 400 mAh/g after 100 cycles [9]. Rakesh et al. proposed an in-situ carbon coated $CuCo_2S_4$ ($CuCo_2S_4$/C) anode to solve this capacity fading issue. However, the capacity of $CuCo_2S_4$/C is also reduced from 1065 (1^{st} discharge) to 296 (30^{th} discharge) mAh/g at 137 mA/g [12]. Therefore, poor cycling performance, which is caused by the capacity fading effect, is a major problem that needs to be addressed for the practical use of metal sulfides as LIB anode materials [24]. Figure 1 and Table S1 shows the comparative

electrochemical LIBs performance of our $CuCo_2S_4$-rGO anode with other Cu/Co-bases anodes [8-14].

Herein,

we report the facile hydrothermal synthesis of a graphene-integrated $CuCo_2S_4$ hybrid composite material as an anode for LIBs. In comparison with the pristine $CuCo_2S_4$ anode material, the $CuCo_2S_4$-reduced graphene oxide ($CuCo_2S_4$-rGO) hybrid composite anode demonstrated significantly improved battery performance without capacity fading. The incorporation of graphene into $CuCo_2S_4$ plays a key role in enhancing the electronic conductivity as well as terminating the active material dissolution through discharge/charge reactions, resulting in superior Li^+ storage and long-life cyclability.

2. Experimental methods

Analytical grade chemical reagents were purchased from Sigma Aldrich and directly used in the experiments without any further purification. In a typical synthesis, 50 mg of graphene oxide (GO) was dispersed into 50 mL of ethanol by ultrasonic treatment for 1 hour (h). Initially, 4.89 mmol of $Cu(NO_3)_2 \cdot 3H_2O$, 4.15 mmol of $Co(NO_3)_2 \cdot 6H_2O$, and 51.67 mmol of thiourea (CH_4N_2S) were dissolved in 60 mL of ethanol, followed by the addition of 31.22 mmol of urea (CH_4N_2O). Then, the GO dispersion was added to the mixture solution with vigorous stirring for 30 min at room temperature (figure 2(a; A)). The mixture solution was then transferred to a 100 mL Teflon-lined hydrothermal synthesis autoclave reactor (figure 2(a; B)) and heated at 150 °C for 12 h. After natural cooling (figure 2(a; C)), the $CuCo_2S_4$-rGO precipitate was collected by centrifugation, washed several times with ethanol, and vacuum-dried at 80 °C (figure 2(a; D)).

For comparison purposes, pure $CuCo_2S_4$ was also synthesized using the same synthesis procedure without the addition of GO into the mixture solution [6,27].

An X-ray diffractometry technique was used to characterize the structural properties of the samples by Cu-K_α radiation (λ = 1.54056 Å, Rigaku Smartlab) at 40 kV with an applied current of 30 mA. The Raman spectra of the samples were taken by LabRam Aramis (Horiba Jobin Yvon) with an Ar-ion laser beam (λ = 514.5 nm). The morphological and compositional properties of $CuCo_2S_4$ and $CuCo_2S_4$-rGO were characterized by field emission scanning electron microscopy (FE-SEM) and energy dispersive X-ray spectroscopy (EDX; Model: JSM-6701F; Japan). Transmission electron microscopy (TEM, JEOL-3000F) images, high-resolution TEM (HR-TEM) images, and selected-area electron diffraction (SAED) patterns were obtained at 300 kV.

The working electrodes were fabricated using a doctor-blade method. The active material ($CuCo_2S_4$ or $CuCo_2S_4$-rGO; figure S1(a)), carbon black (conductive additive), and polyvinylidene fluoride (PVDF) binder were mixed in N-methyl 1-pyrrolidone (NMP) with a mass ratio of 80:10:10 to form anode slurry. This slurry was coated on a copper foil current collector (figure S1(b)) and vacuum dried in an oven at 80 °C. The electrochemical performance of the anode materials for LIBs was evaluated using coin-type half-cells (CR2032, figure S1(c)). The test cells were assembled in an argon-filled glove box. The coated copper foil {15 mm disc; loaded with $CuCo_2S_4$ (1.62 mg) or $CuCo_2S_4$-rGO (1.67 mg)} and lithium metal foil served as the working and counter/reference electrodes, respectively, and a single-layer polypropylene membrane (Celgard 2400) was used as the separator. A 1 M $LiPF_6$ solution in a solvent mixture of diethylene carbonate (DEC) and ethyl carbonate (EC) was used as the electrolyte (DEC/EC in a 1:1 volume ratio).

The electrochemical behavior of the samples was characterized by cyclic voltammetry (CV), galvanostatic charge/discharge (GCD), and electrochemical impedance spectroscopy (EIS) measurements. CV measurements were carried out in a potential window of 0.005-3.000 V (vs. Li/Li^+) at different scan rates ranging from 0.1 to 5 mV s^{-1}, and the cells were discharged/charged galvanostatically at a various current densities ranging from 0.1 to 2 A g^{-1} using a battery cycler (Bio-Logic Scientific Instruments, France). The electrochemical impedance spectroscopy (EIS) measurements were performed in a frequency range of 1-10 kHz.

3. Results and Discussion

The structural phase of the $CuCo_2S_4$-rGO hybrid composite material was characterized by X-ray diffraction (XRD). The representative XRD patterns of GO, $CuCo_2S_4$, and $CuCo_2S_4$-rGO are shown in figure 2(b). As expected, GO exhibited a strong and sharp diffraction peak centered at 11.6°, which corresponded to the reflection of the (001) plane [28]. A broad peak around 21° corresponded to the (002) plane, which may be associated with a small domain of coherent and parallel stacking of graphene sheets [29,30]. The XRD spectra of $CuCo_2S_4$ and $CuCo_2S_4$-rGO had diffraction peaks at 31.30°, 38.06°, 47.2°, 50.08°, 54.90°, and 57.60°, which corresponded to the reflection of the (113), (004), (224), (115), (044), and (135) planes of carrollite $CuCo_2S_4$ (JCPDS card no. 42-1450), respectively. On the other hand, for the hybrid $CuCo_2S_4$-rGO sample, the graphene peak at 11.6° was not detected, which may be attributed to the hybridization of graphene with $CuCo_2S_4$. However, the presence of graphene in the hybrid composite was revealed in a Raman spectrum. Figure 2(c) shows the Raman spectra of the GO, $CuCo_2S_4$, and $CuCo_2S_4$-rGO samples. The Raman peak around 265 cm^{-1} may be assigned to the vibrational mode of a Cu-S bond [27,31]. The two peaks at 356 and 658 cm^{-1} corresponded to Co-S bonds,

and the peak at 474 cm^{-1} may be associated with the S-S symmetric stretching mode (A_{1g}) of the covalent S-S bond [27,32]. Therefore, the observed Cu-S, S-S, and Co-S Raman signals indicated the formation of $CuCo_2S_4$. Moreover, the Raman spectrum of the GO sample showed two broad peaks at ~ 1360 cm^{-1} (D-band) and at 1587 cm^{-1} (G-band), which may be associated with the vibrational lattice motion (A_{1g} symmetry of *k* point phonon) away from the Brillouin zone and the stretching mode (E_{2g} symmetry of phonons) of sp2 carbon atoms [33-36]. The $CuCo_2S_4$-rGO sample demonstrated an increased I_D/I_G intensity ratio (~ 0.99), which was higher than that of the GO (~ 0.88) powder sample. The increased I_D/I_G intensity ratio of the hybrid compound sample may be attributed to the formation of new and smaller sp2 domains caused by the reduction of GO to rGO during the hydrothermal process [9,37], suggesting the hybridization of $CuCo_2S_4$ and rGO. Moreover, the near-surface chemical binding states were estimated by performing XPS measurement, the XPS spectrum (figure S2) analysis confirmed the Cu^{2+}, Co^{3+}, and S^{2-} oxidation states of the constituent elements of $CuCo_2S_4$ phase for both pristine and composite samples.

FE-SEM images of the $CuCo_2S_4$ (figures 3(a) and (b)) and $CuCo_2S_4$-rGO (figures 3(c) and (d)) samples revealed a micro-spherical morphology with an average diameter of ~ 600 nm. For the $CuCo_2S_4$-rGO sample, micro-spheres were encapsulated with graphene nanosheets, as indicated by a red-dashed circle (figure 3(d)). The main constituent elements (Co, Cu and S) were confirmed via EDX measurements (figures S3(a) and (b)). As expected, an additional carbon (C) peak was observed in the EDX spectrum of the $CuCo_2S_4$-rGO sample, which further confirmed the presence of graphene nanosheets. In addition, elemental mapping of the $CuCo_2S_4$-rGO sample showed the uniform distribution of the Cu, Co, S, and C elements (figures 3(e-h)) with ~13.51% of graphene in the $CuCo_2S_4$-rGO composite sample (see inset of figure S3(b)).

Raman, XPS, FE-SEM, and EDX analyses consistently demonstrated that the graphene nanosheets were well incorporated into $CuCo_2S_4$, forming a $CuCo_2S_4$-rGO hybrid composite material.

The microscopic structure of the samples was examined by TEM. Figure 4(a) shows the TEM image of the hybrid $CuCo_2S_4$-rGO sample (for the pristine $CuCo_2S_4$, see figure S4(a) in Supporting Information), which revealed the formation of a spherical morphology. The phase and crystallinity of the materials were examined by HR-TEM, as shown in figures 4(b) and S4(b). Locally oriented lattice fringes (outlined by colored boxes) were detected, and their lattice distances were indexed. The hybrid $CuCo_2S_4$-rGO compound had d-spacing values of 0.34 ± 0.1 nm and 0.20 ± 0.1 nm, which were indexed to the (022) and (224) planes, respectively. The pristine $CuCo_2S_4$ sample also had two clear lattice fringes, which corresponded to the (022) and (113) planes (see figure S4(b) in Supporting Information). Figure 4(c) shows the SAED patterns of the $CuCo_2S_4$-rGO composite (see figure S4(c) in Supporting Information for the pristine $CuCo_2S_4$), and the overlap of the discrete irregular spots with grey and black diffused rings confirmed the polycrystalline nature of the $CuCo_2S_4$ and $CuCo_2S_4$-rGO samples. The observed spots were indexed to the reflections of the (044), (224), (113), (022), and (111) planes. The result of SAED pattern analysis were consistent with HR-TEM data.

The presence of graphene (C), Cu, Co, and S in the graphene-integrated $CuCo_2S_4$ sample was confirmed at the atomic scale by energy-dispersive spectroscopy scanning TEM (EDS-STEM) mapping. Figures 4(d) and S4(d) show the measured EDS-STEM line scan along the direction indicated in the image (figure 4(d)). The three core elements (Cu, Co, and S) were detected in both samples; however, the graphene (C) signal was only observed for the composite sample. The line profile shapes of both samples were almost similar, suggesting that the C signal

originated from the integrated graphene of the hybrid $CuCo_2S_4$-rGO composite material and not only from the background, which was supported by EDX analysis (extracted data plot, figure 3(f)). Two-dimensional elemental mapping (figures 4(e-j) and S4(e-i)) revealed that the constituent elements were uniformly distributed.

Figures 5(a) and (b) show the five consecutive CV curves of the $CuCo_2S_4$ and $CuCo_2S_4$-rGO electrodes at a scan rate of 0.1 mV s^{-1} (For the pristine GO anode, the measured CV plot is shown in figure S5(a).). The 1st CV cycle of the electrodes had clear oxidation and reduction peaks that are described as follows [38]:

$$CuCo_2S_4 + 8\ Li^+ + 8\ e^- \leftrightarrow 4\ Li_2S + 2\ Co + Cu \quad (2)$$

$$Li_2S \leftrightarrow 2\ Li^+ + 2\ e^- + S \quad (3)$$

$$Co + Li_2S \leftrightarrow CoS + 2\ Li^+ + 2\ e^- \quad (4)$$

$$Cu + Li_2S \leftrightarrow CuS + 2\ Li^+ + 2\ e^- \quad (5)$$

$$CoS + 1/3\ Li_2S \leftrightarrow 1/3\ Co_2S_3 + 2/3\ Li^+ + 2/3\ e^- \quad (6)$$

The reduction peaks of the $CuCo_2S_4$ electrode at ~ 1.0, 1.2, and 1.56 V (vs Li/Li^+) in the 1st cathodic sweep may be associated with multistep electrochemical reactions. The cathodic peak at 1.0 V (vs. Li/Li^+) may be associated with the formation of the solid electrolyte interphase (SEI) layer and the decomposition of the electrolyte [39]. The oxidation peaks at ~ 2.0 and ~ 2.3 V (vs. Li/Li^+) in the 1st anodic potential sweep may be assigned to the Cu^{2+} lithiation process and the conversion of Li_2S into sulfur (S) and Li^+, respectively [12]. In the 2nd CV curve, the cathodic peak at 1.2 V (vs. Li/Li^+) originated from the initial insertion of Li^+ to form Li_2S, and this peak was subsequently shifted towards ~ 1.27 V (vs. Li/Li^+). This cathodic peak may be attributed to the lithiation process or reduction of Co^{2+} or Co^{3+} to Co metal [9-13]. The other reduction peak at

around 1.56 was shifted towards ~ 1.6 V (vs. Li/Li^+), which corresponded to the decomposition of the lithiated electrode to form a stable phase of Cu or Co metal [9,13,38]. Figure 5(b) shows the CV curves of the hybrid $CuCo_2S_4$-rGO anode; only two reduction peaks at ~ 1.0 and 1.27 V (vs. Li/Li^+), and two oxidation peaks at ~ 2.0 and ~ 2.3 V (vs. Li/Li^+) were observed in the 1st CV sweep. In the 2nd CV sweep, two reduction peaks were observed at ~ 1.27 and 1.6 V (vs. Li/Li^+), which were almost similar to those of the $CuCo_2S_4$ anode; however, the fading trend was much weaker than that of the $CuCo_2S_4$ anode. This is presumably associated with the fact that the graphene incorporation suppresses the dissolution of metal sulfide species into the organic electrolyte and effectively increases the surface capacitive contribution due to the increased contact area between the electrolyte and the electrode. The wettability and hydrophobicity of the hybrid anode material are enhanced in the organic electrolyte after graphene integration [40]. The incorporated graphene is expected to be chemically stable during the Li interaction/deintercalation process and it prevents the metal sulfide species from being dissolved into the electrolyte.

Figures 5(c) and (d) show the five-consecutive discharge/charge curves of the anode materials at a current density of 0.1 A g^{-1} (figure S5(b) displays the discharge/charge profile for the pristine GO anode). The 1st specific discharge and charge capacities of the pristine $CuCo_2S_4$ anode were 627 and 689 mAh g^{-1} {coulombic efficiency (η) of 91%}, respectively, whereas those of the $CuCo_2S_4$-rGO anode were of 802 and 822 mAh g^{-1} {η = 91.5%}, respectively, at the same current density. The $CuCo_2S_4$-rGO anode delivered higher 1st cycle capacity with enhanced coulombic efficiency. The capacities of both anodes were significantly decreased at the 2nd discharge (429 and 729 mAh g^{-1} for the $CuCo_2S_4$ and $CuCo_2S_4$-rGO anodes, respectively). The decrease in capacity at the 2nd cycle may be attributed to SEI layer formation on the surface of

the electrode/electrolyte interface. After the 5th cycle, the pristine $CuCo_2S_4$ anode delivered a discharge capacity of only 145 mAh g^{-1} {η = 95%} due to capacity fading. This capacity fading behavior is consistent with CV data. On the other hand, the hybrid $CuCo_2S_4$-rGO composite anode retained a discharge capacity of 667 mAh g^{-1} after the 5th cycle. The coulombic efficiency was increased from 1st to 5th cycle and maintained ~ 99% in the subsequent cycles. The observed capacity fading in both the charge and discharge processes was much weaker for the hybrid composite anode compared with the pristine $CuCo_2S_4$ anode; this is because the incorporated graphene (rGO) that provides flexible structure to hybrid anode and prevent capacity fading during lithiation/de-lithiation.

Figure 6(a) shows the rate capability of the pristine $CuCo_2S_4$ and $CuCo_2S_4$-rGO anodes at different current densities. The specific capacity of the $CuCo_2S_4$ and $CuCo_2S_4$-rGO anodes at 0.1 A g^{-1} was 627 and 802 mAh g^{-1}, respectively. In the initial 5 cycles at 0.1 A g^{-1}, the specific capacity of the $CuCo_2S_4$ anode faded rapidly due to volume expansion or dissolution of the anode material into the electrolyte. On the other hand, the $CuCo_2S_4$-rGO anode had higher capacity values at all current densities, and capacity fading during the 1st five cycles was considerably weaker for the $CuCo_2S_4$-rGO anode compared with the pristine $CuCo_2S_4$ anode. When the driving current return at 0.2 A g^{-1} the $CuCo_2S_4$-rGO anodes restore the capacity of almost 87%. The decrease in capacity restoration might be result of slightly deformed material structure.

The high-rate and long-term cycle stability of an anode is essential for practical LIB applications. Figure 6(b) shows the measured specific capacity of the $CuCo_2S_4$ and $CuCo_2S_4$-rGO anodes at 0.2 A g^{-1} as a function of the cycle number. The pristine $CuCo_2S_4$ anode delivered a discharge capacity of 345 mAh g^{-1} at 0.2 A g^{-1} (figure 6(b)), and it was decreased sharply to

148 mAh g^{-1} after the 20th cycle; this indicated capacity fading in the charge/discharge processes (figure 5(c)). On the other hand, the graphene-integrated $CuCo_2S_4$ anode delivered a discharge capacity of 490 mAh g^{-1} at the same current density of 0.2 A g^{-1}. The initial decrease in capacities of both $CuCo_2S_4$ and $CuCo_2S_4$-rGO anodes is associated with fading effect, however, the fading trend in composite anode was poor because of graphene-integration. The faded capacity was then recovered (~ 80-100 cycles) might be related to material activation after the reversible growth of a polymeric gel-like film catalyzed by 3d metals [41], but the regain trend in the pristine $CuCo_2S_4$ anode was poor compared with graphene-integrated $CuCo_2S_4$ anode. The capacity retention after the 500th cycle at 0.2 A g^{-1} was ~ 82% for the $CuCo_2S_4$-rGO hybrid composite anode but only ~ 30% for the pristine $CuCo_2S_4$ anode. This analysis is consistent with the CV results measured after the stability test (see figure S6). The reliability of these results was further confirmed by evaluating the LIB performance of these anode materials at the same testing conditions. The $CuCo_2S_4$-rGO retained the capacity value within a tolerable limit (see figure S7 in Supporting Information). Figure 6(c) shows the long-term cycle stability of the hybrid $CuCo_2S_4$-rGO anode at different current densities. The hybrid composite anode exhibited excellent cycle stability even at a very high current density of 2.0 A g^{-1} with a capacity retention of 52% and a coulombic efficiency of ~ 99%. Moreover, the structural phase after the stability test (figure S8(a), see Supporting Information) were in good agreement with the proposed electrochemical reaction mechanism. The material morphology (figure S8(b)) and the composition (figure S8(c)) were almost unchanged, suggesting the superior endurance of the $CuCo_2S_4$-rGO throughout the stability cycles.

Reaction kinetics can be determined from quantitative CV analysis. The scan rate-dependent CV curves of the $CuCo_2S_4$ and $CuCo_2S_4$-rGO anodes are shown in figures 7(a) and (b).

Figure 7(c) shows the log-log plots of the cathodic current (i) and scan rate (v) for the $CuCo_2S_4$-rGO anode at various potential values (figure S9(a) shows similar plots for the $CuCo_2S_4$ anode). The extracted log (i) vs. log (v) plots obey a power-law relationship that can be expressed as follows [41-43]:

$$J = a \times v^{b}, \tag{7}$$

where a and b are fitting parameters. The b-value is between 0.45 and 1.0. If the b-value is ~ 0.5 the current is controlled by semi-infinite linear diffusion [41]. However, if the b-value is close to 1.0, the measured current originates from the interface or surface-capacitive controlled process [41]. Figure 7(d) shows the calculated b-values at various potentials, which varies between 0.5 and 1.0, suggesting that both Li^+ intercalation and surface capacitance could contribute to the measured current. As the cathodic potential increases, the b-value decreases, reaching a minimum at 1.5 V (vs. Li/Li^+) before it increases. Therefore, at a potential of 1.5 V (vs. Li/Li^+), at which the b minima are formed, the dominant capacitance originates from the Li^+ intercalation (diffusion) process at the electrode/electrolyte interface [41]. Beyond the characteristic potential of 1.5 V (vs. Li/Li^+), the energy storage process changes from the Li^+ intercalation process to a surface-controlled process. The measured current can be expressed at a fixed potential as a combination of the surface capacitive effects ($k_1 \cdot v$) and the Li^+ diffusion-controlled insertion process ($k_2 \cdot v^{1/2}$) [41-45]:

$$i(v) = k_1 \cdot v + k_2 \cdot v^{1/2}, \tag{8}$$

where k_1 and k_2 are adjustable fitting parameters. For analytical purposes, Eq. (8) is rearranged as

$$J(v)/v^{1/2} = k_1 \cdot v^{1/2} + k_2\,, \tag{9}$$

Figure 8(a) shows the $J/v^{1/2}$ vs. $v^{1/2}$ curves for the $CuCo_2S_4$-rGO anode at various cathodic potentials (figure S9(b) shows similar plots for the $CuCo_2S_4$ anode). By calculating k_1 and k_2, it is possible to determine the relative percentage ratio of the capacitive and diffusive contributions to the observed current at various scan rates [41], as shown in figure 8(b). The surface capacitance contribution was increased with increasing scan rate. Figures 8(c) and (d) show the surface capacitance contribution (shaded region) and diffusive contribution (unshaded region) in the CV curves at 0.1 mV s^{-1} and 5 mV s^{-1}, respectively, for the $CuCo_2S_4$-rGO anode (for the $CuCo_2S_4$ anode, see figures S9(c) and (d) in Supporting Information). The superior capacitive Li^+ storage capacity of the $CuCo_2S_4$-rGO anode may be attributed to a larger non-Faradaic contribution, which may be associated with the enhancement of the interfacial double-layer capacitance by the integrated graphene.

EIS measurements were performed to elucidate the intrinsic electron transfer kinetics of the anode materials [5,46-48]. Nyquist plots of the pristine $CuCo_2S_4$ and $CuCo_2S_4$-rGO anodes before and after 500 cycles are shown in figure 9(a). The inset shows the equivalent circuit. In the low-frequency region, the slope of the linear portion of the Nyquist curve represents the Warburg impedance (W) [5,6], which corresponded to the linear diffusion of Li^+ in the anode material. The point of the intersection of the curve with the X-axis represents the internal resistance (R_s). In the high-frequency region, the semicircle (figure 9(b)) represents the charge transfer resistance (R_{ct}) at the anode/electrolyte interface attributed to the Faradaic reaction. R_{SEI} and CPE1 are the resistance and constant phase element, respectively, which may be associated with the formation of an SEI layer on the electrode surface. Table S2 shows the parameter values determined from simulating the measured EIS spectra. The $CuCo_2S_4$-rGO anode demonstrated improved Li^+ conduction compared with the pristine $CuCo_2S_4$ because of its superior electrical

conductivity, which may result from the integration of graphene. Even after 500 stability cycles, the R_{ct} value of the $CuCo_2S_4$-rGO anode was increased slightly from 41 to 51 Ω, whereas that of the pristine $CuCo_2S_4$ anode was markedly increased from 75 to 136 Ω. This significant change in the R_{ct} value may be attributed to either material dissolution or polysulfide formation during discharge/charge processes.

4. Conclusions

We demonstrated the hydrothermal synthesis of a graphene-integrated $CuCo_2S_4$ composite as an anode material for LIBs. The incorporation of graphene considerably enhanced the Li^+ storage properties and sustainability of pristine $CuCo_2S_4$ anode. The hybrid $CuCo_2S_4$-rGO composite anode exhibited a 1st specific discharge capacity of 802 mAh g^{-1} at 0.1 A g^{-1}. It also demonstrated an excellent capacity retention of 82% after 500 stability cycles at 0.2 A g^{-1}; in contrast, the pristine $CuCo_2S_4$ anode demonstrated a capacity retention of only 30%. Moreover, the $CuCo_2S_4$-rGO anode demonstrated a good capacity retention of 64 and 52% at a high current density of 1.0 and 2.0 A g^{-1}, respectively, after 500 stability discharge/charge cycles. Besides, quantitative CV analysis revealed that the Li^+ storage mechanism can be defined by both surface capacitive effects and the diffusion-controlled insertion process. EIS analysis indicated that the substantially improved battery performance of the graphene-integrated $CuCo_2S_4$ anode was attributed to the incorporation of graphene, which could prevent material dissolution in the electrolyte and polysulfide formation during charge/discharge processes.

Acknowledgments

The authors would like to thank the financial support from the National Research Foundation (NRF) of Korea (Grant nos. 2018R1A2B6007436, 2016R1A6A1A03012877, 2018R1D1A1B07049046, 2018R1D1A1A09083859).

References

[1] Goriparti S, Miele E, Angelis F D, Fabrizio E D, Zaccaria R P, and Capiglia C 2014 *J. Power Sources* **257** 421

[2] Jin R, Yang L, Lia G, and Chen G 2015 *J. Mater. Chem. A* **3** 10677

[3] Xiao J, Choi D, Cosimbescu L, Koech P, Liu J, and Lemmon J P 2010 *Chem. Mater.* **22** 4522

[4] Kong D, He H, Song Q, Wang B, Lv W, Yang Q H, and Zhi L 2014 *Energy Environ. Sci.* **7** 3320

[5] Ahmed A T A, Hou B, Chavan H S, Jo Y, Cho S, Kim J, Pawar S M, Cha S, Inamdar A I, Kim H, and Im H 2018 *Small* **14** 1800742

[6] Ahmed A T A, Chavan H S, Jo Y, Cho S, Kim J, Pawar S M, Gunjakar J L, Inamdar A I, Kim H, and Im H 2017 *Journal of Alloys and Compounds* **724** 744

[7] Ahmed A T A, Pawar S M, Inamdar A I, Kim H S, and Im H 2019 *Adv. Mater. Interfaces* **7** 1901515

[8] Wang P, Zhang Y, Yin Y, Fan L, Zhang N, and Sun K 2018 *ACS Appl.* **10** 11708

[9] Zheng T, Li G, Meng X, Li S, and Ren M 2019 *Chem. Eur. J.* **25** 885

[10] Nie L, Wang H, Chai Y, Liu S, and Yuan R 2016 *RSC Adv.* **6** 38321

[11] Qu B, Li H, Zhang M, Mei L, Chen L, Wang Y, Li Q, and Wang T 2011 *Nanoscale* **3**, 4389

[12] Verma R, Kothandaraman R, and Varadaraju U V 2017 *Applied Surface Science* **418** 30

[13] Cheng J, Pan Y, Zhu J, Li Z, Pan J, and Ma Z 2014 *J. Power Sources* **257** 192

[14] Lai C, Huang K, Cheng J, Lee C, Hwang B, and Chen L 2010 *J. Mater. Chem*. **20** 6638

[15] Gong Y, Zhao J, Wang H, and Xu J 2018 *Electrochimica Acta* **292** 895

[16] Kim T H, Song H K, and Kim S 2019 *Nanotechnology* **30** 275603

[17] Zhang X, Li S. El-Khodary S A, Zou B, Yang S, Ng D H L, Liu X, Lian J, and Li Huaming 2020 *Nanotechnology* **31** 145404

[18] Zhang J, Zhao Y, Zhang Y, Li J, Babaa M R, Liu N, and Bakenov Z 2020 *Nanotechnology* **31** 095405

[19] Xie W, Wang Q, Wang W, Xu Z, Li N, Li M, Jia L, Zhu W, Cao Z, and Xu J 2019 *Nanotechnology* **30** 325405

[20] Gao Y, Li J, Wang L, Hou Y, Lai X, Zhang W, Chen X, Zhang P, Huang Y, and Yue B 2019 *Nanotechnology* **31** 055705

[21] Chen Z, Du Y, Zhang Z, Gao T, and Li H 2019 *Nanotechnology* **30** 495403

[22] Mahmood N, Zhang C, Jiang J, Liu F, and Hou Y 2013 *Chem. Eur. J.* **19** 5183

[23] Li L, Kovalchuk A, Fei H, Peng Z, Li Y, and Kim N D 2015 *Adv. Energy Mater*. **5** 1500171

[24] Mahmood N, Tang T, and Hou Y 2016 *Adv. Energy Mater*. **6** 1600374

[25] Cheon S. Ko K, Cho J, Kim S, Chin E, and Kim H 2003 *J. Electrochem. Soc*. **150** A800

[26] Liang C, Dudney N J, and Howe J Y 2009 *Chem. Mater*. **21** 4724

[27] Ahmed A T A, Pawar S M, Inamdar, A I, Im H, and Kim H S 2020 *Int. J. Energy Res.* **44** 1798

[28] Chen F, Jia D, Jin X, Cao Y, and Liu A 2016 *Dyes and Pigments* **125** 142

[29] Zhang K, Zhang Y, and Wang S 2013 *Scientific Reports* **3** 3448

[30] Rosi M, Ekaputra M P, Iskandar F, Abdullah M, and Khairurrijalal 2010 *AIP Conference Proceedings* **86** 1325

[31] Milekhin A G, Yeryukov N A, Sveshnikova L L, Duda T A, Rodyakina E E, Gridchin V A, Sheremet E S, and Zahn D R T 2015 *Beilstein J. Nanotechnol.* **6** 749

[32] Givalou L, Antoniadou M, Perganti D, Giannouri M, Karagianni C S, Kontos A G, and Falaras P 2016 *Electrochimica Acta* **210** 630

[33] Zhu J, Zhu T, Zhou X, Zhang Y, Lou X W, Chen X, Zhang H, Hng H H, and Yan Q 2011 *Nanoscale* **3** 1084

[34] Velasquez P, Leinen D, Pascual J, Ramos-Barrado J R, and Grez P 2005 *J. Phys. Chem. B* **109** 4977

[35] Wang Y, Alsmeyer D C, and McCreery R 1990 *Chem. Mater*. **2** 557

[36] Shen J, Hu Y, Shi M, Lu X, Qin C, Li C, and Ye M 2009 *Chem. Mater*. **21** 3514

[37] Jhonsi M A, Nithya C, and Kathiravan A 2014 *Phys. Chem. Chem. Phys*. **16** 20878

[38] Nie L, Wang H, Liu S, and Yuan R 2016 *Chalcogenide Letters* 2016 **13** 555

[39] Zhou Y, Yan D, Xu H, Liu S, Yang J, and Qian Y 2015 *Nanoscale* **7** 3520

[40] Vinayan B P, Nagar R, Raman V, Rajalakshmi N, Dhathathreyan K S, and Ramaprabhu S 2012 *J. Mater. Chem.* **22** 9949

[41] Ahmed A T A, Hou B, Inamdar A I, Cha S N, Kim H, and Im H 2019 *Energy technology* **7** 1900295

[42] Lukatskaya M R, Dunn B, and Gogotsi Y 2016 *Nature Communication* **7** 12647

[43] Wang J, Polleux J, Lim J, and Dunn B 2007 *J. Phys. Chem. C* **111** 14925

[44] Wang R, Lang J, Zhang P, Lin Z, and Yan X 2015 *Adv. Funct. Mater.* **25** 2270

[45] Inamdar A I, Ahmed A T A, Chavan S H, Jo Y, Cho S, Kim J, Pawar S M, Hou B, Cha S N, Kim H, and Im H 2018 *Ceramics International* **44** 18625

[46] Pawar S M, Pawar B S, How B, Ahmed A T A, Chavan H S, Jo Y, Cho S, Kim J, Seo J, Cha S N, Inamdar A I, Kim H, and Im H 2019 *J. Ind. Eng. Chem.* **69** 13

[47] Sankar S, Lee H, Jung H, Kim A, Ahmed A T A, Inamdar A I, Kim H, Lee S, Im H, and Kim D 2017 *New J. Chem.* **41** 13792

[48] Cho S, Kim J, Jo Y, Ahmed A T A, Chavan S H, Woo H, Inamdar A I, Gunjakar J L, Park Y, Kim H, and Im H 2017 *J. Alloys and Compound* **725** 108

Figures

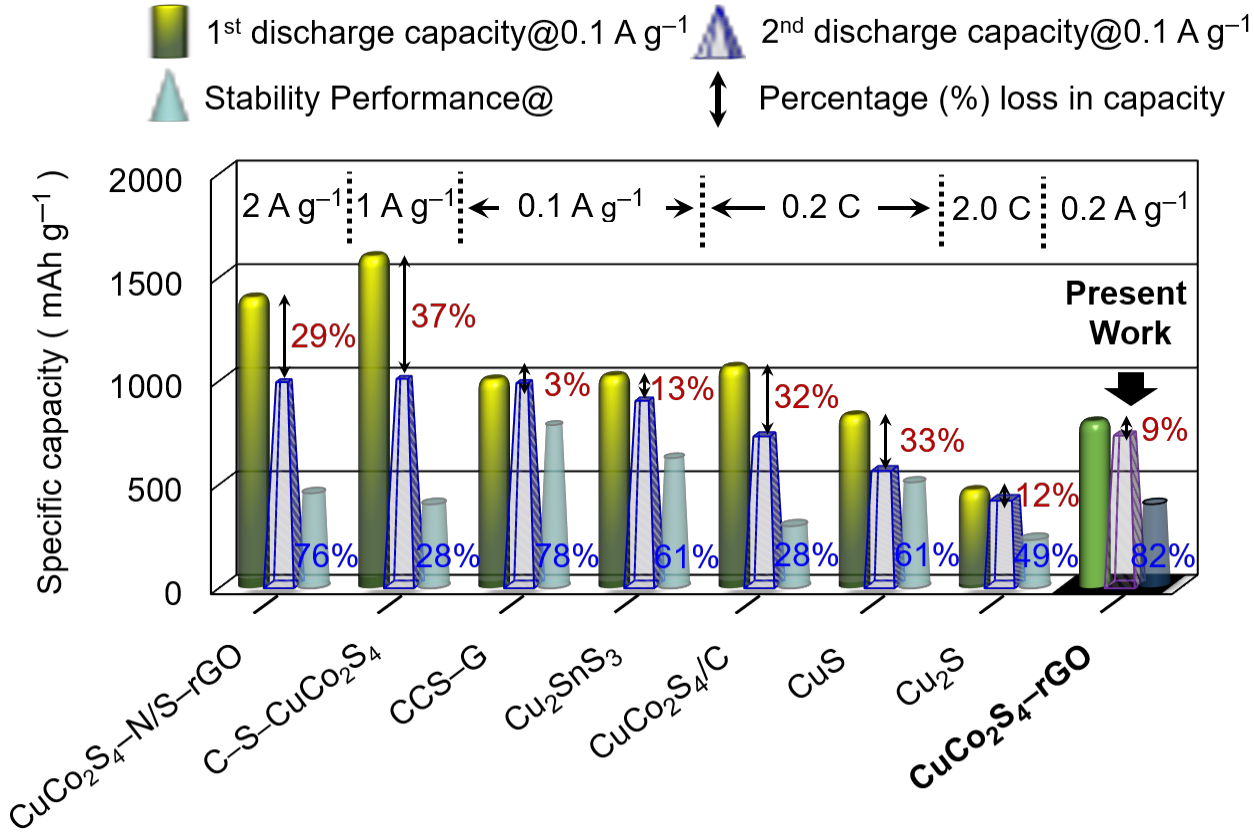

Figure 1. LIBs performances of our $CuCo_2S_4$-rGO (graphene integrated) anode and other Cu/Co-based sulfide anodes such as $CuCo_2S_4$-N/S-rGO [8], C-S-$CuCo_2S_4$ (Core-shell) [9], CCS-G (Flower-like) [10], Cu_2SnS_3 [11], $CuCo_2S_4$/C (carbon coated) [12], CuS [13], and Cu_2S (nanowire array) [14]. Note that the electrochemical LIBs performance reported at different current rates and stability cycle number (≥ 100 cycles, except for the $CuCo_2S_4$-N/S-rGO and C-S-$CuCo_2S_4$ reported for 500 and 1000 cycles, respectively). However, the survey compares the problem aroused with sulfide-based anodes, such as capacity loss between 1st and 2nd cycle due to SEI layer formation and gradual capacity fading during stability cycle. The double-sided vertical arrow indicates the loss in capacity between 1st and 2nd discharge. Stability performance represents the last cycle discharge capacity and assigned number stands for the capacity retention at the end of stability cycles. Notably, the CCS-rGO anode possesses lowest capacity loss after SEI film formation and highest capacity retention of 82% after 500 cycles.

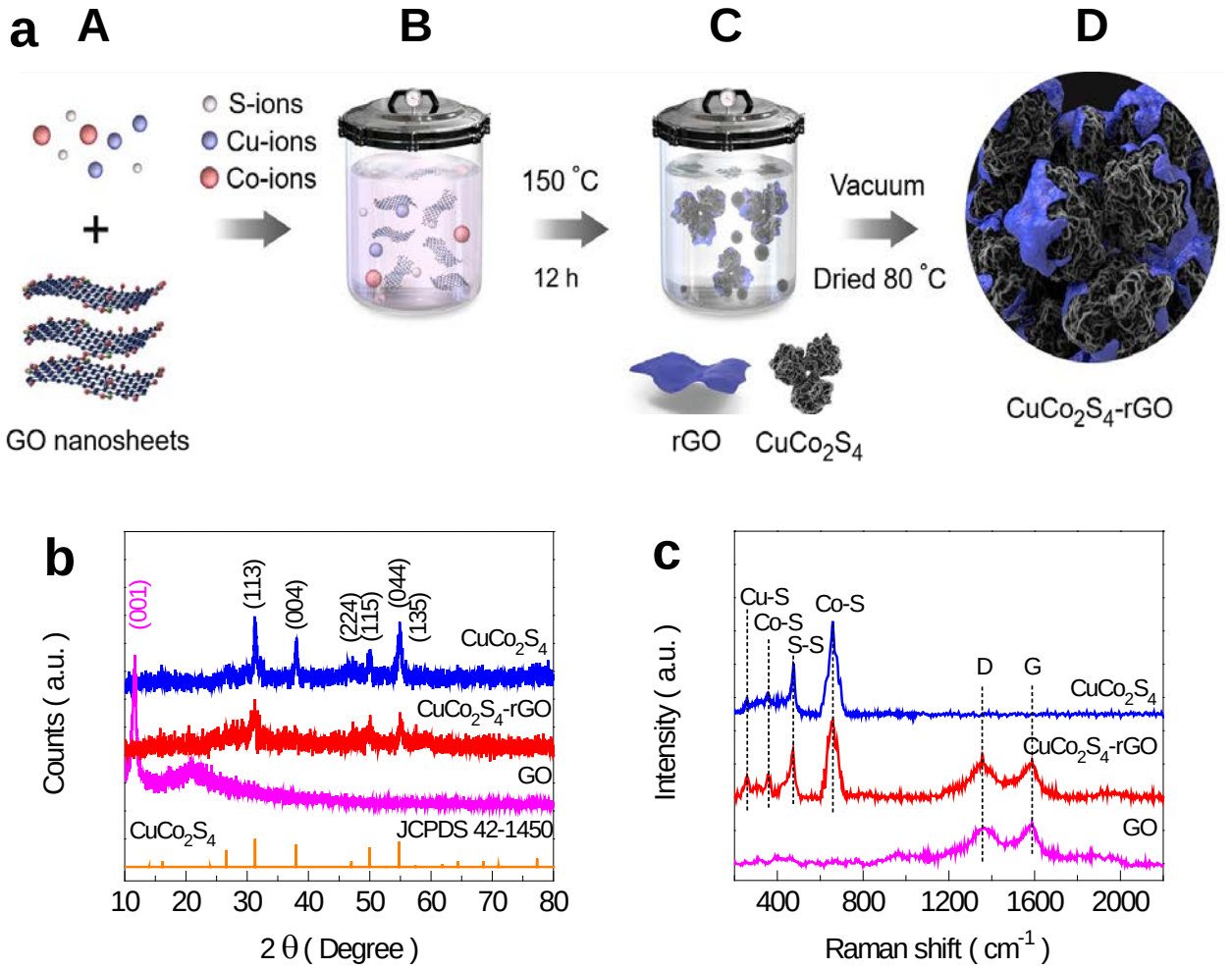

Figure 2. Schematic illustration of $CuCo_2S_4$-rGO hybrid composite synthesis via a facile hydrothermal technique. (a; A) Stoichiometric molar ratios of copper, cobalt, and sulfur ion sources were mixed in ethanol followed by the addition of pre-dispersed graphene oxide under strong stirring. (a; B) This mixture solution is then transferred to Teflon-lined stainless-steel autoclave reactor for hydrothermal synthesis. (a; C) As obtained $CuCo_2S_4$-rGO powder after natural cooling to room temperature. (a; D) Vacuum dried integrated graphene structure of the $CuCo_2S_4$ micro-sphere. Two-dimensional sheets (blue) represent the graphene sheet, and the spheres represent the $CuCo_2S_4$ particle. These spheres were wrapped with graphene sheet during hydrothermal synthesis. (b) XRD with the relevant JCPDS card number. (c) Raman spectra of GO, pristine $CuCo_2S_4$, and $CuCo_2S_4$-rGO. The XRD and Raman spectra are colored from magenta to red.

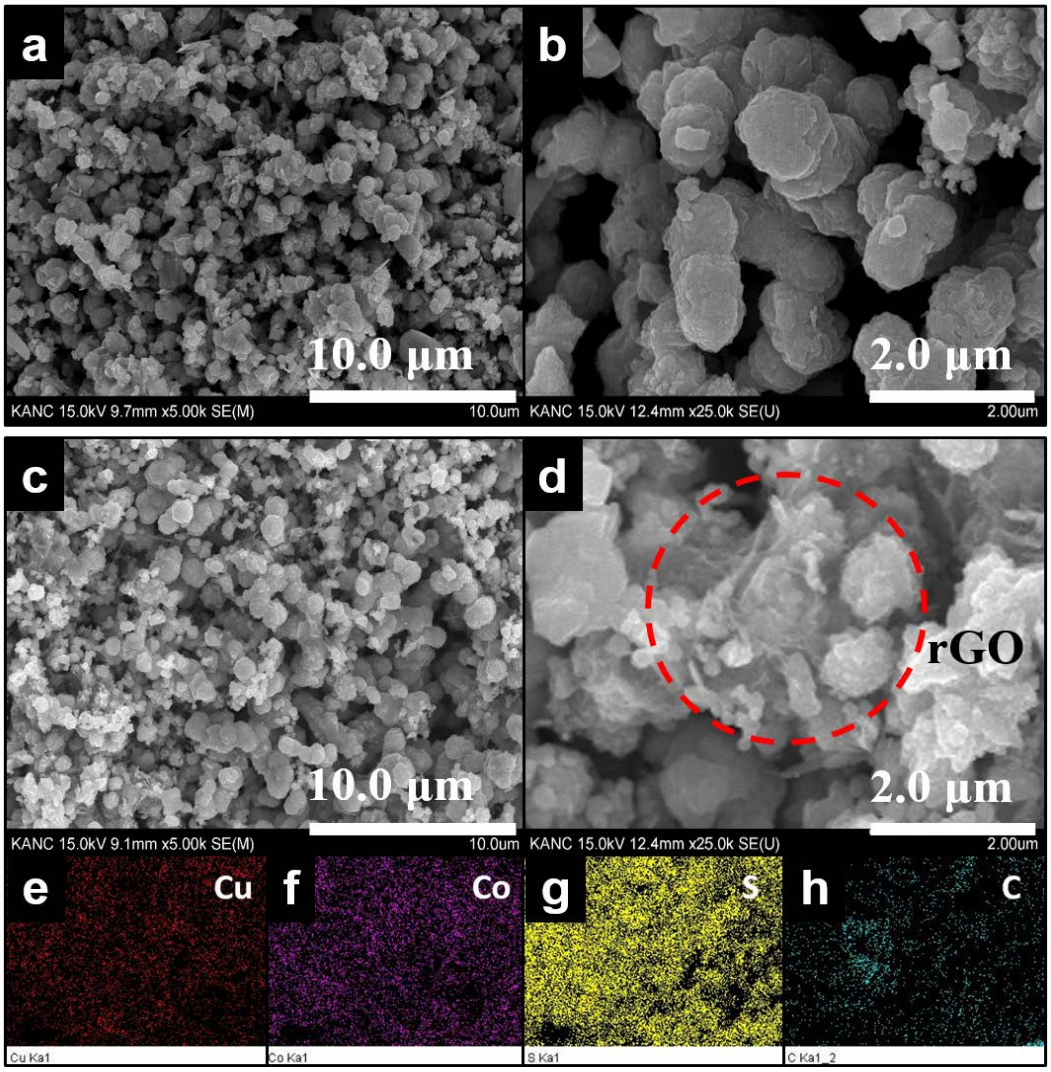

Figure 3. FE-SEM images of the (a and b) $CuCo_2S_4$ and (c and d) $CuCo_2S_4$-rGO. Elemental mapping of $CuCo_2S_4$-rGO revealed the uniform distribution of the (e) Cu, (f) Co, (g) S, and (h) C elements.

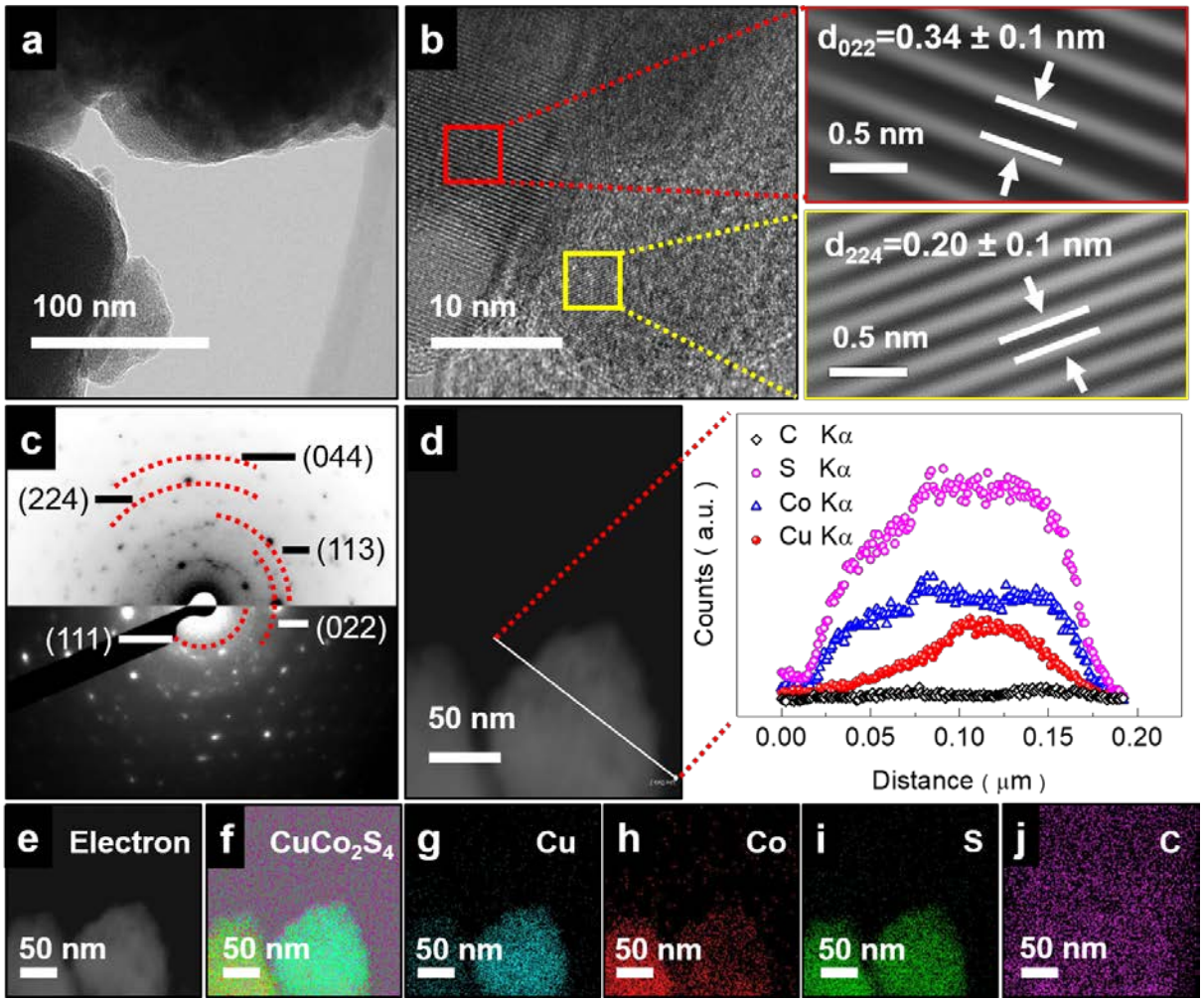

Figure 4. (a) TEM image, (b) HR-TEM image, (c) SAED (ring pattern outlined with red-dotted curves). (d) EDS-STEM line mapping (white line across the sphere), (e) EDS-STEM image and the corresponding two-dimensional elemental mapping of the (f) composite, (g) Cu, (h) Co, (i) S, and (j) C elements of the $CuCo_2S_4$-rGO.

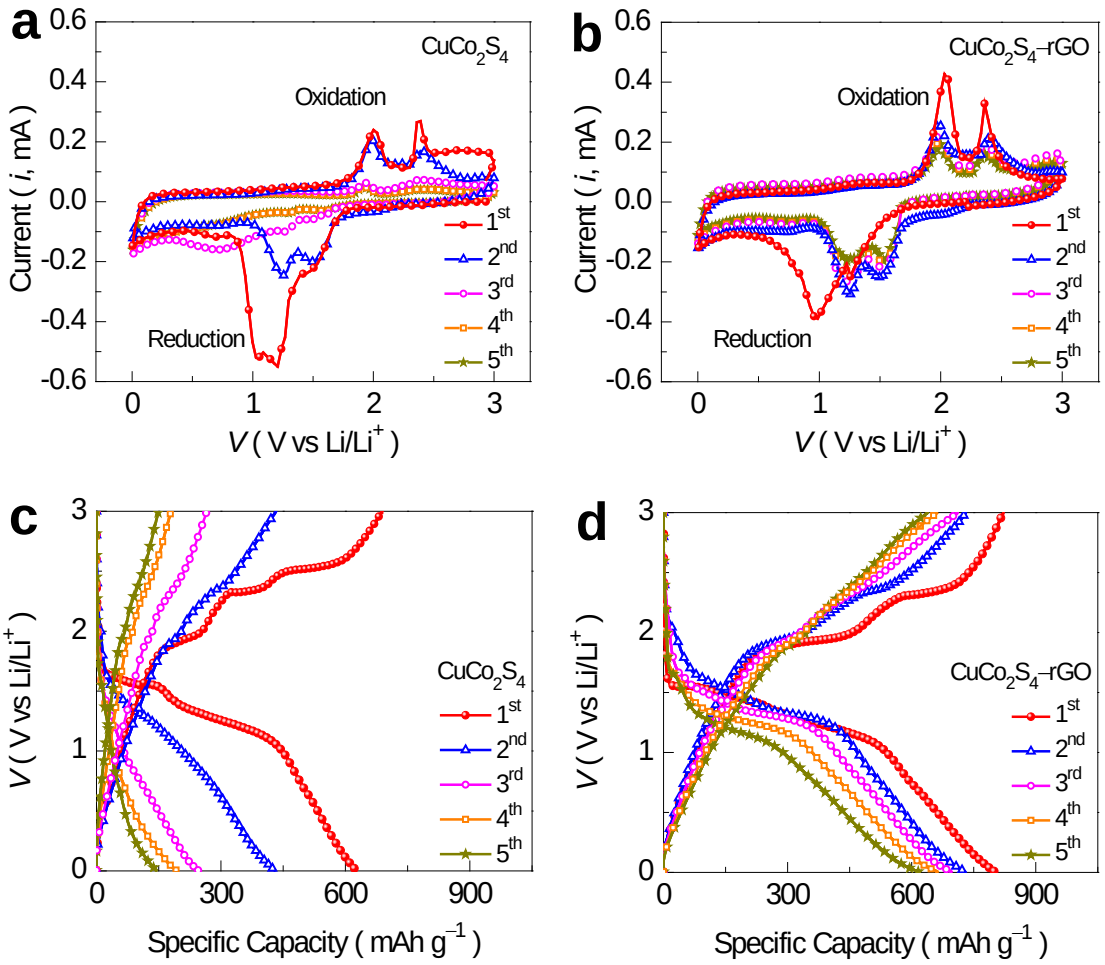

Figure 5. (a) Initial five CV cycles of (a) pristine $CuCo_2S_4$ and (b) $CuCo_2S_4$-rGO composite at 0.1 mV s^{-1}. Initial five discharge/charge curves of (c) pristine $CuCo_2S_4$ and (d) $CuCo_2S_4$-rGO at a current density of 0.1 A g^{-1}. The CV and discharge/charge curves are colored from red to dark-yellow and each curve is distinguished by different symbols such as red solid-sphere (1^{st}), blue open-triangle (2^{nd}), magenta open-circle (3^{rd}), orange open-square (4^{th}), and dark-yellow filled-star (5^{th}).

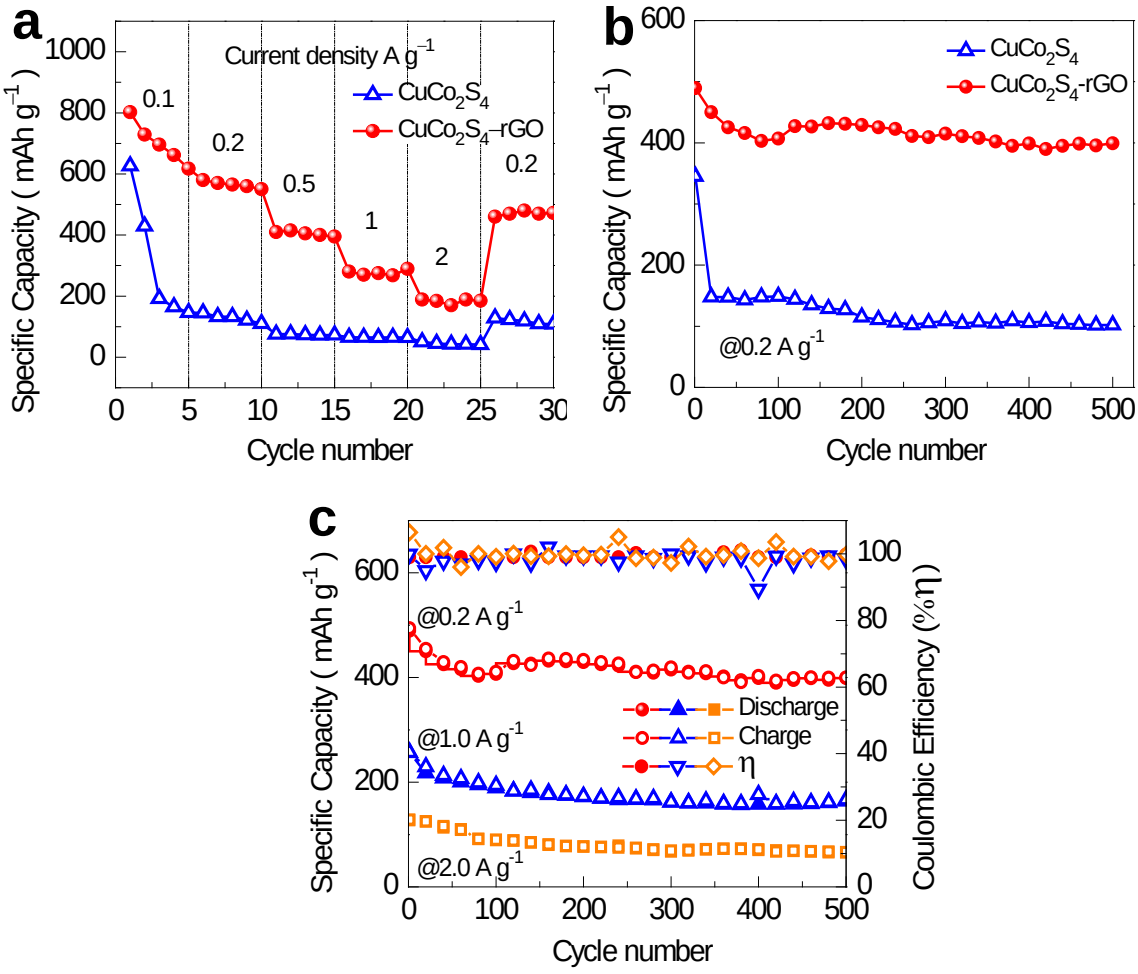

Figure 6. (a) Capacity restoration capability at various current densities and (b) 500 discharge/charge stability cycles of the pristine $CuCo_2S_4$ and $CuCo_2S_4$-rGO hybrid composite anodes. (c) Effect of current density performance on the sustainability of the $CuCo_2S_4$-rGO anode over 500 stability cycles.

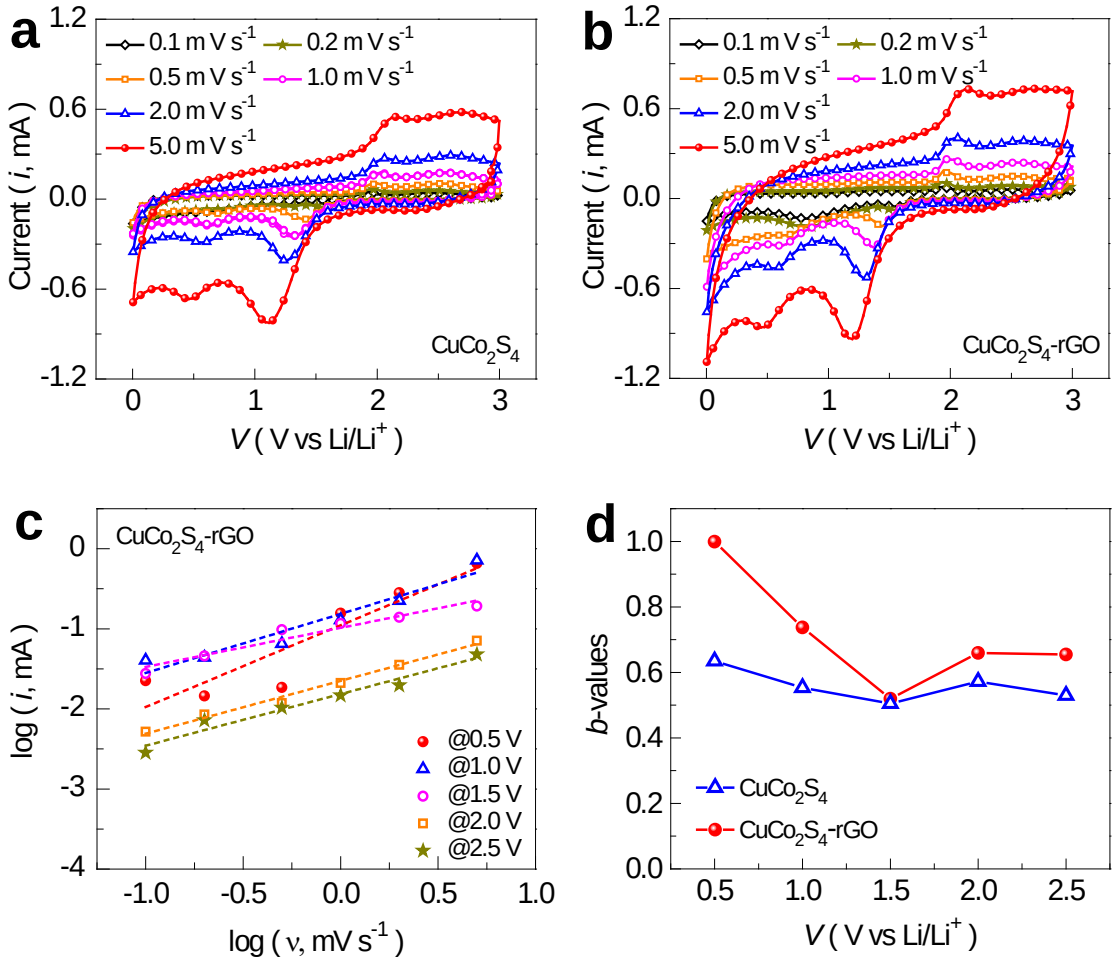

Figure 7. (a) Scan rate-dependent CVs of the (a) $CuCo_2S_4$ and (b) $CuCo_2S_4$-rGO hybrid composite anodes. (c) Power-law dependence of current density as a function of the scan rate in the cathodic region between 0.5 and 0.25 V (vs. Li/Li^+) using Eq. (7) demonstrated good linearity. (d) *b*-values of the $CuCo_2S_4$-rGO anode plotted as a function of the potential V (vs. Li/Li^+) for cathodic scans.

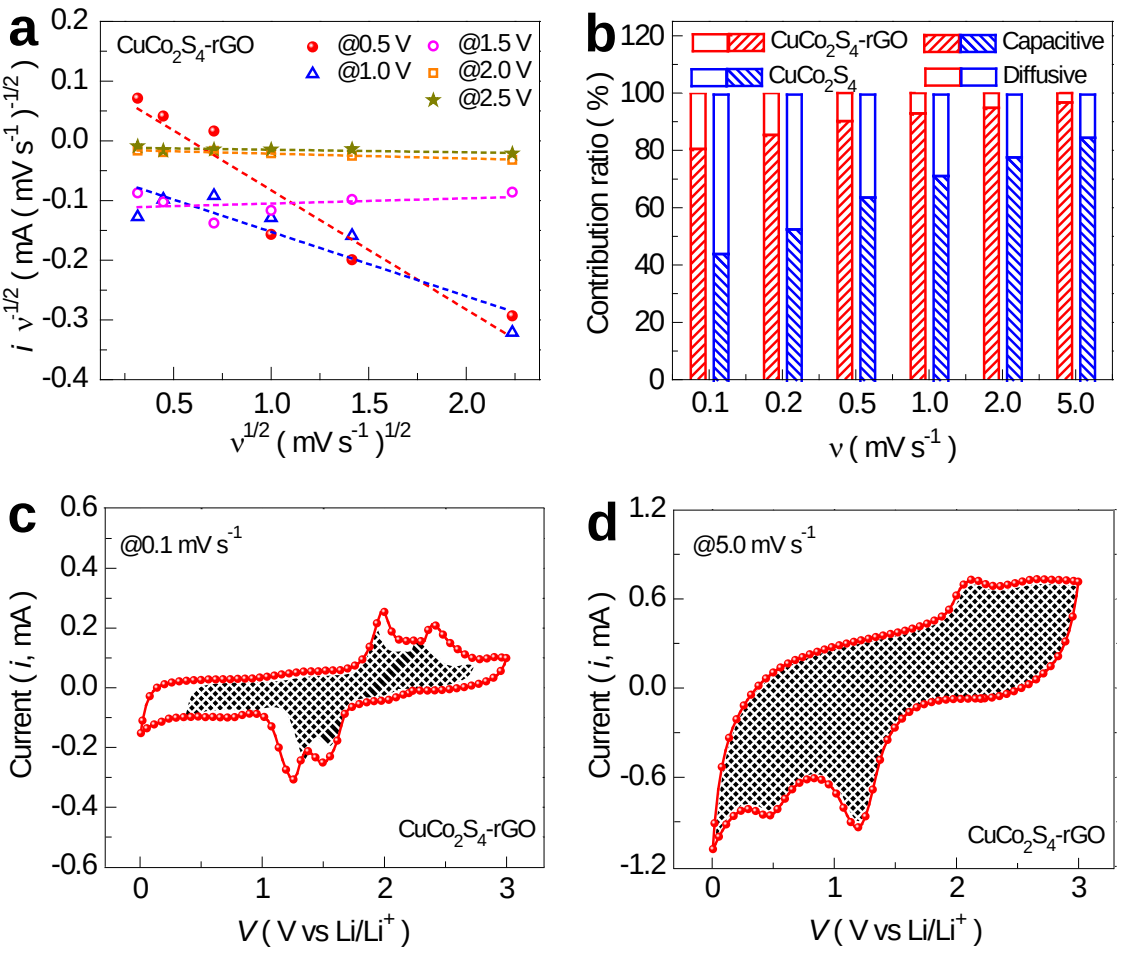

Figure 8. (a) Analysis of the cathodic CV data for the $CuCo_2S_4$-rGO anode using Eq. (9). Sweep rates were ranged from 0.1 to 5.0 mV s^{-1}. (b) Comparison of charge storage for the $CuCo_2S_4$-rGO anode. The total charge was separated into Li^+ intercalation and capacitive contributions. CV curves of the $CuCo_2S_4$-rGO anode at (c) 0.1 and (d) 5.0 mV s^{-1}. The red solid line (total current) was obtained experimentally. The capacitive current (black shaded regions) and diffusive current (remaining space between the solid line and shaded area) were determined from the data in figure 7(b).

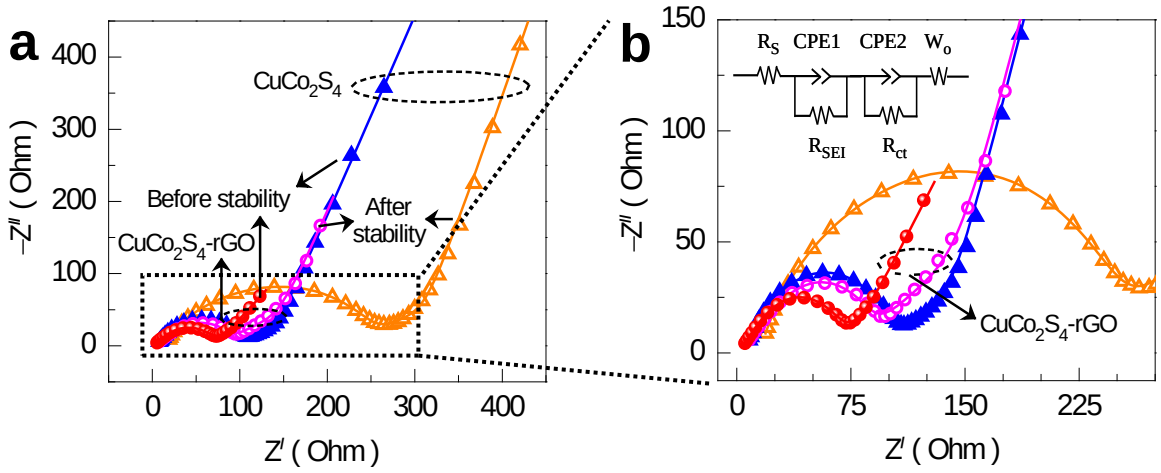

Figure 9. (a) Nyquist plots of the pristine $CuCo_2S_4$ and $CuCo_2S_4$-rGO anodes before and after 500 discharge/charge stability cycles. (b) The magnified view revealed a clear difference between each semicircle with their equivalent simulated circuit. The filled circle (red) and filled triangle (blue) represent the EIS plots before stability test for $CuCo_2S_4$-rGO and the pristine $CuCo_2S_4$ anodes, respectively, whereas the open circle (magenta) and open triangle (orange) stand for the $CuCo_2S_4$-rGO and the pristine $CuCo_2S_4$ anodes after the stability test, respectively. EIS plots of both anodes before and after stability testing are marked with arrow.